





Original Paper

Validation, verification, and quality control of computational fluid dynamics analysis for indoor environments using a computer-simulated person with respiratory tract

Sung-Jun Yoo  and Kazuhide Ito 

Faculty of Engineering Sciences, Kyushu University, Japan

*Correspondence

Sung-Jun Yoo, Faculty of Engineering Sciences, Kyushu University, Japan.
Email: yoo@kyudai.jp

Funding information

Japan Science and Technology Corporation, Grant/Award Number: JP20356547; Japan Society for the Promotion of Science, Grant/Award Number: JP20KK0099, JP21K14306, JP21KD2002, JP22H00237; Ministry of Education, Culture, Sports, Science and Technology, Grant/Award Number: JPMXP1020210316; Taisei Foundation, Grant/Award Number: 20015

Received September 8, 2022; Accepted September 18, 2022

doi: 10.1002/2475-8876.12301

Abstract

Computer-simulated persons (CSPs) with respiratory systems have been developed for microclimate analysis around the human body and inhalation exposure analysis, for detailed assessment of comfort and health risks in indoor spaces. This study examined and validated the prediction accuracy of a CSP, for precise estimation of indoor environmental quality (IEQ). The flow-field prediction accuracy was thoroughly examined in a grid analysis using the CSP and a thermal manikin for benchmarking. The model incorporated unsteady breathing and human postural sway, and assessed their impact on the microclimate around the human body. The numerically estimated flow field was validated using experimental particle image velocimetry (PIV) data, with a detailed grid independence test. Considering the practical use of the respiratory tract model for the inhalation exposure risk assessment, the prediction accuracy of particle transport and deposition analysis was examined using previously published in vivo experimental results. This analysis revealed that the impact of transient breathing and body vibrations on the reproduction of the thermal plume around the human body is quite weak; consequently, these conditions can be ignored from the macroscopic perspective of indoor airflow analysis.

Keywords

computational fluid dynamics, computer simulated person, human micromotion, indoor environmental quality assessment, validation and verification

1. Introduction

Indoor environmental quality (IEQ) significantly affects the quality of life (QOL), as people in contemporary societies tend to spend most of their time indoors. In particular, the indoor air quality and thermal environment are key factors that affect human health, comfort, and productivity. For better design of indoor environments, much attention has been devoted to the methods for predicting their quality and its impact on humans; these studies typically target the entire indoor space as well as the local environment around the human body.

Several experimental studies targeting indoor environments have been conducted up to date, yielding information that can be used to improve their design. Here, humans constitute the most important factor for designing indoor environments;

consequently, many experiments have used thermal manikins and experimental subjects, allowing detailed and successful investigations of interactions between humans and indoor environments in which they dwell. However, these studies have suffered from many constraints (such as time, space, and cost of experiments), as well as ethical restrictions associated with subject-involving experiments.

In light of the above, various computer-simulated persons (CSPs) for IEQ assessment have been developed recently, which became possible owing to great strides in the computational sciences. Early on, relatively simple geometries, such as cylinders and cuboids, were used for computational human models. Xing et al. investigated the distribution of contaminants around a seated human, using experimental data and computational fluid dynamics (CFD) analysis based on a

thermal manikin and a four-cuboid CSP model.¹ Brohus et al. used three cuboid human models, for estimating the exposure of humans to contaminants in ventilated indoor spaces.^{2,3} In addition to these cuboid models, many non-cuboid CSPs with simplified human body geometry were developed and used for estimating the flow, temperature, and contaminant distributions around humans.^{4–6} While simple-geometry CSPs have been favored owing to their smaller computational demands, Topp et al. pointed out that more realistic geometries better predict the airflow distribution around the human body.⁷ They have investigated the differences between the CFD results for cuboid CSPs and realistic-geometry CSPs; while there was little or no impact on the global indoor climate, a noticeable effect was observed in the CSP proximity. These results suggest the need for the development of realistic-geometry CSPs, for more accurate numerical analysis of human-centered health risks and thermal comfort. This has motivated the development of various realistic-geometry CSPs.^{8–12}

For establishing a comprehensive IEQ predictive model using realistic “digital twins” of humans, it is necessary to reproduce not only the detailed shape of the human body but also the fundamental physiological functions of the human body that potentially affect the indoor climate. A typical example is the heat generation owing to the thermoregulation of the human body. The human body is a significant source of heat, owing to its metabolic activity that maintains the body temperature in the physiological range. The humans’ thermal environment significantly affects their heat loss and thermal comfort in indoor spaces; in turn, human thermoregulation affects the indoor thermal environment. Capturing this interaction between humans and their indoor environments is key to CSP-based human microclimate analysis. The most visible impact of the human heat generation in indoor spaces is a convective updraft around the human body, which creates a complex flow pattern in the surrounding indoor space and thus may affect the transport of contaminants, increasing human health risks. In addition, a recent study, using CSP-based numerical analysis, suggested that the contaminant inhalation probability can be affected by human-generated thermal plumes.¹³ In view of the above, methods that enable high-accuracy predictions of thermal plumes around humans are necessary for precise estimation of IEQ.

At the same time, indoor air quality can significantly affect human health and comfort, because air is vital to humans. Many previous studies have investigated inhalation-related health risks, using numerical analysis techniques and computational modeling of the human respiratory tract and the breathing process.^{14–20} Moreover, many studies have focused on the integrated analysis (combining indoor spaces and the respiratory tract) and its application to indoor environmental design.^{12,21,22} A comprehensive prediction method accounting for the local indoor climate, microclimate around the human body, and contaminant transfer in the respiratory zone under continuous breathing, is needed for elucidating the indoor contaminant transfer mechanisms and associated human health risks owing to respiratory exposure and airborne infections.

Another key function of the human body that is correlated with indoor climate and human health is body movement. The human body is not stationary, and various movements associated with daily activities are essential for maintaining routine life. In addition to these active movements of the human body, there is an ever-present micromotion resulting from a postural control scheme to maintain the stability and orientation of the human body with humans in upright standing/sitting positions.

This can be seen as postural sway owing to the torque variation at the ankles, knees, and hip joints, exercised by neural control pathways. It is widely known that the postural sway angle is age- and health condition-dependent;²³ at the same time, certain-intensity postural sway may influence the microclimate around the human body and convective heat loss from the skin. However, none of the previous studies have focused on this aspect, while some have investigated the impact of walking on the microclimate around the human body and contaminant transfer characteristics in indoor spaces.^{3,6,12,23–27} Reproducing regular micromotion of the human body in the IEQ assessment using a realistic body geometry would be more generalizable than the ability to reproduce specific movements of the human body, allowing to discuss in detail the environmental effects of micromotion under static conditions.

This study introduces an originally developed CSP that uses a realistic human body geometry, including the respiratory tract components from the nasal/oral cavity to the bronchial tubes. Benchmark grid tests of the CSP were performed to establish a method for predicting the local/global climate around the human body and in the respiratory tract in the CFD framework. The feasibility of the human microclimate analysis capturing thermal plumes, breathing patterns, and human micromotion was examined, and the reproducibility of in vivo particle deposition experiments in the respiratory tract is discussed to provide useful information on the quality control of indoor CFD-based CSP simulations.

2. Verification and Validation of the CSP

To accurately evaluate the IEQ and environmental interactions between humans and indoor climates using CSPs, it is essential to precisely reproduce a complex flow field around a detailed human body geometry, including the thermal plume owing to the human heat generation. This paper introduces a verification and validation process targeting the global/local airflow distribution around the human body, which is the dominant factor in human-centered heat and contaminant transfer.

2.1 Outline of the CSP

This study used the CSP that was originally developed in our previous studies.^{28,29} There are six types of CSPs: adult male, adult female, and child models in standing and seated postures. The CSP of an adult male model in the standing posture was used for examining the prediction accuracy of the method in this study. A sophisticated human body geometry was reproduced based on the representative human body scale of Japanese males, and the complex geometry of the fingers and toes was simplified to reduce the calculation load.

Figure 1 shows the geometry and grid design of the CSP that was used in this study. The surface meshes were arranged using 56 000 polygonal meshes (size range, 0.5 to 345.5 mm²). Considering the health risk and thermal comfort assessment based on the human microclimate analysis, it is highly important to accurately predict the heat/contaminant behavior on the CSP surface. To accurately predict the flow profile in the viscous sublayer based on the wall function of the turbulence model, 10 layers of boundary meshes were created near the CSP surface. The height of the first cell was 0.2 mm; as a result, the non-dimensional distance from the CSP surface (y^+) was confirmed based on Equation (1) to be below 1.0, over the entire CSP surface and for the airflow approaching at 1.0 m/s. Here, y_1 is the normal distance between the first cell centroid and the CSP surface, and ν is

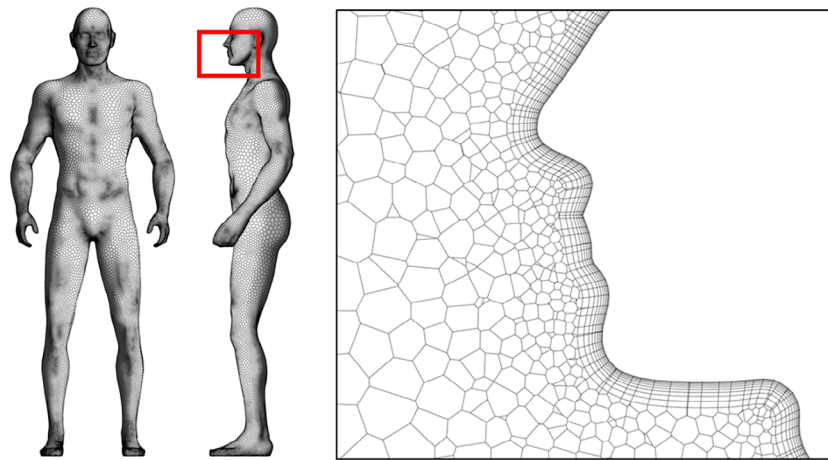


FIGURE 1. Surface meshes on the CSP and 10 layers of boundary cells near the CSP surface

the air kinematic viscosity. u^* denotes the friction velocity, and is given by Equation (2). ρ and τ_w represent the air density and surface shear stress, respectively.

$$y^+ = u^* y_1 / \nu, \tag{1}$$

$$u^* = \sqrt{\tau_w / \rho}. \tag{2}$$

To verify the indoor climate analysis using the CSP, grid independence tests were performed using various grid designs. By examining the discrepancies between the results obtained using the different grid designs, and focusing on the scalar velocity distribution around the CSP, the optimal grid was determined. Finally, a benchmark test for validating the CSP analysis was performed using the measured data of global/local velocity and temperature obtained from an environmental chamber experiment that used a thermal manikin.

2.2 Grid independence tests of the CSP

In this study, six different grid designs were considered for examining the precision of calculations in the CSP proximity. Across these grid designs, the grid resolution parameter, R^* [-], varied from 4 to 28.³⁰ The grid resolution was determined by Equation (3), using a representative cell size, $\max(\delta x, \delta y, \delta z)$ [m], and the characteristic length of the domain, L [m], defined by the domain volume V [m³] and domain total surface area A

[m²]. Figure 2 shows the representative grid designs used in the grid independence tests. The tests estimated the calculation error of the flow-field analysis in the CSP proximity, which fundamentally affects the heat and mass transfer analysis; therefore, variations in the grid designs with various grid densities in the CSP proximity were considered. Identical designs for the surface meshes and boundary layer meshes on the CSP were used in each of the grid designs.

$$R^* = \frac{L}{\max(\delta x, \delta y, \delta z)}, \tag{3}$$

$$L = \frac{V}{A}. \tag{4}$$

A simple model room was created for the grid independence tests, as shown in Figure 3A, and the CSP was positioned at the center of the model room. Flow-field analysis using the shear-stress transport (SST) $k-\omega$ turbulence model³¹ was conducted, assuming uniform airflow (0.1 m/s) from the anterior to posterior region. To reproduce a complex flow pattern with a thermal plume around the human body, the CSP surface temperature and ambient airflow temperature were set to 33.55°C and 24.85°C, respectively. For quality control of the CFD analysis using the CSP, analytical methods suggested in previous studies were carefully considered.³²⁻³⁹ The second-order

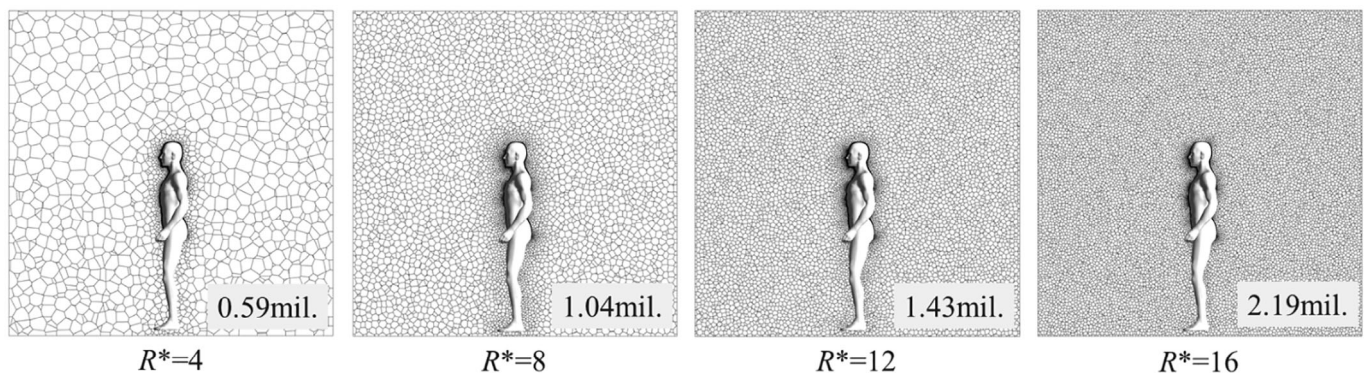


FIGURE 2. Grid designs in the CSP proximity, with the representative grid resolution R^* varying from 4 to 16

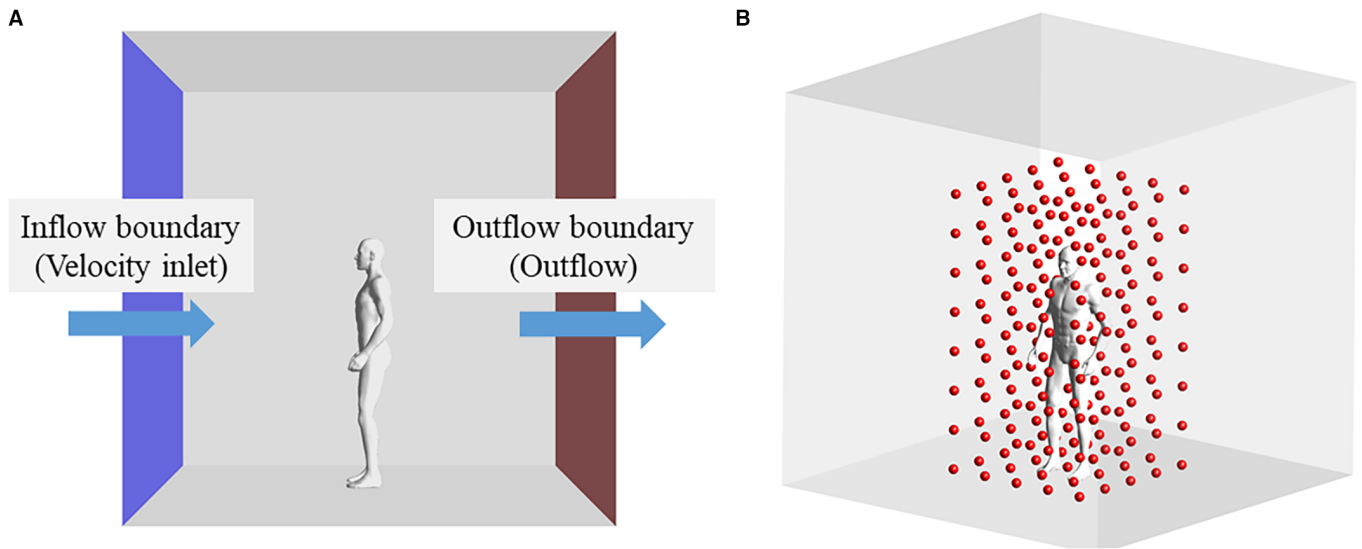


FIGURE 3. (A) A simple model room with the CSP and (B) the spatial loci of the data points sampled for the error analysis

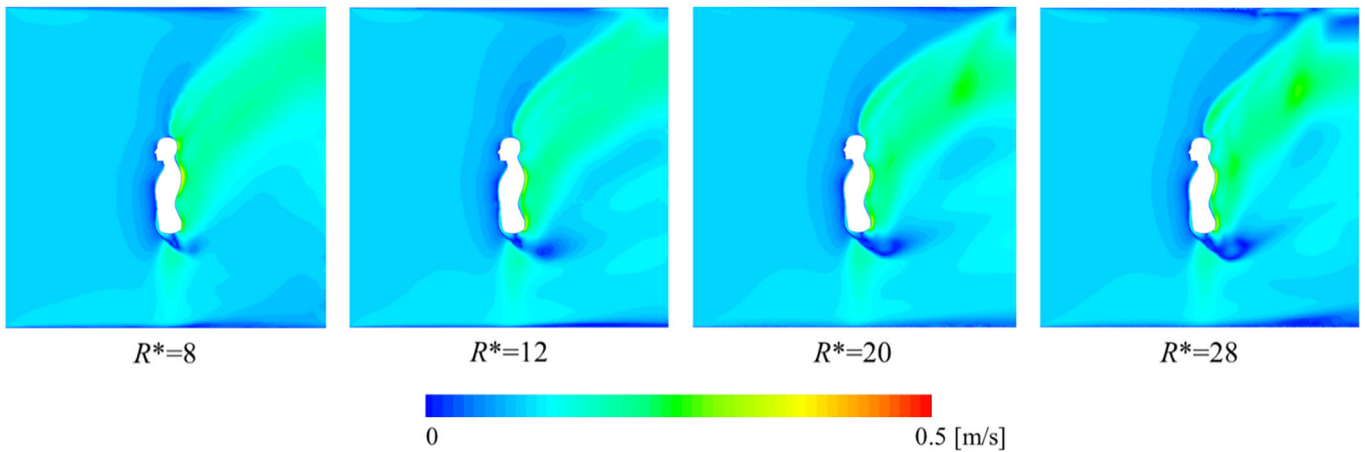


FIGURE 4. Scalar velocity distributions around the CSP

upwind scheme was used for the convection term, and the SIMPLE algorithm was used.

For the calculation error analysis, scalar velocity values were sampled from equally spaced 200 points (distance, 0.3 m) in the CSP-centered cuboid region, as shown in Figure 3B. In this study, the data obtained for the densest grid design of $R^* = 28$ were considered as reference data, and the coefficient of variation of the root mean square error (CV(RMSE)) and coefficient of determination (R^2) were estimated for each grid design.

The analysis results of the scalar velocity distribution around the CSP are shown in Figure 4, for the representative grid resolutions of $R^* = 8, 12, 20,$ and 28 . All of the considered grid designs clearly yielded non-uniform and complex distributions around the realistic-geometry CSP, and no significant differences between the velocity scale and flow patterns of thermal plumes were observed across the different grid resolutions, while small discrepancies between flow patterns were observed in some local domains.

The analysis results of CV(RMSE) and R^2 for the different grid designs are summarized in Table 1. In this study, a grid design was considered optimal if its associated CV(RMSE)

TABLE 1. Results of the error analysis, for the different considered grid resolutions

Grid resolution R^*	Grid number	Volume-average Velocity [m/s]	CHTC on CSP [W/m ² K]	CV(RMSE)	R^2
28	7 938 170	0.1070	3.68	—	—
24	5 320 567	0.1064	3.68	3.64%	0.98
20	3 443 538	0.1064	3.69	15.08%	0.71
16	2 191 801	0.1063	3.71	15.28%	0.70
12	1 429 864	0.1067	3.68	9.52%	0.88
8	1 040 619	0.1068	3.65	11.77%	0.82
4	581 950	0.1130	3.62	19.08%	0.53

was at or below 10% and if its associated R^2 was at or above 0.85; these cutoffs followed Guideline 14 of the American Society of Heating, Refrigerating, and Air-conditioning Engineers (ASHRAE).⁴⁰ The grid design with $R^* = 12$ (the finest grid) exhibited satisfactory results; consequently, it was adopted for the validation tests of the indoor climate analysis

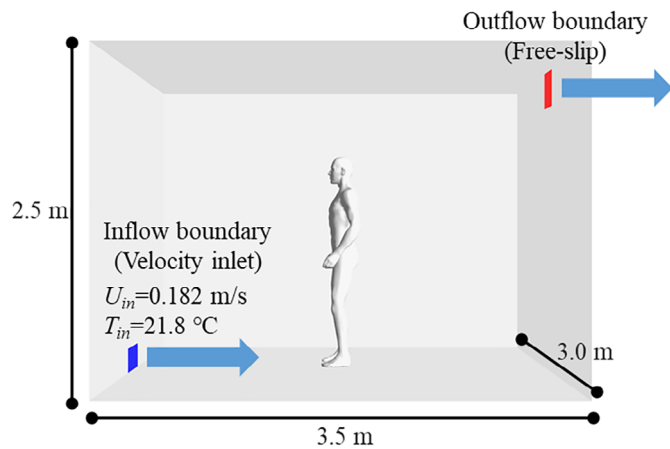


FIGURE 5. Analytical domain for the CSP benchmarking

using the CSP in the present study. The volume-average velocity in the entire domain and the convective heat transfer coefficient on the CSP surface were also calculated for each case, and there were no significant differences between the results obtained for the different grid designs.

2.3 Validation of the flow-field analysis in the CSP proximity

Nielsen et al. reported velocity measurements in an environmental chamber with a thermal manikin.¹¹ To examine the prediction accuracy of the flow pattern in the CSP proximity, benchmarking was performed based on the experimental conditions in the thermal manikin experiment. Figure 5 schematically shows the analytical domain and boundary conditions for the CSP benchmarking. In a model room (dimensions, $3.5 \times 3.0 \times 2.5$ m) the CSP was located at the center, and the boundary conditions for reproducing displacement ventilation were considered. The inflow velocity and temperature were 0.182 m/s and 21.8°C, respectively. The heat generation was identical to that used in the thermal manikin experiment (76 W, convection + radiation), and was applied to the CSP to reproduce the thermal plume around it.

Figure 6 shows the flow-field analysis results for the CSP. Nonuniform and complex flow patterns around the CSP were confirmed, with a clear thermal plume atop the CSP. To

compare the CFD analysis results with the experimental ones, the scalar velocity field was sampled at the same location as the one for which data were sampled in the thermal manikin experiment (line L1-L5), as shown in Figure 6.

Figure 7 summarizes the experimental and CFD analysis-based velocity profiles for lines L1, L2, L4, and L5, revealing good concordance between the two. To investigate the reproducibility of the thermal plume around the human body, the CFD analysis results were compared to the results of particle image velocimetry (PIV) measurements for line L3 (Figure 8). Considering the small geometrical differences between the thermal manikin and the presently used CSP, multiple examinations were performed by sampling from additional points along the anterior-posterior axis from L3 ($z = 1.75$ m). The CFD analysis-based and experimental velocity profiles were very similar. This benchmarking focused on the prediction accuracy of the flow field, which predominantly determines the heat and contaminant transfer in indoor spaces. The above results suggest that sufficient prediction accuracy of global/local climate analysis around the human body can be secured based on the methodology for indoor CFD analysis using the CSP introduced in this study.

3. Reproduction of Human Physiological Functions Using the CSP

3.1 Breathing

Gupta et al. characterized the flow dynamics of breathing and temporal variations in the breathing flow rate.⁴¹ The variation in the breathing flow rate (Q_{res}) can be expressed using the unsteady breathing cycle model defined by Equation (5):

$$Q_{res} = \alpha \sin(\beta t) \quad 5$$

where α and β are the peak flow rate [L/s] and breathing frequency [min^{-1}], which depend on the height, weight, and body surface area of the human body, respectively. In this study, unsteady breathing with a minute volume (MV) of 12.3 L/min was reproduced assuming a standing CSP. As a result, the maximal inhalation and exhalation flow rates reached 0.69 and 0.61 L/s, respectively, as shown at points (a) and (c) in Figure 9. The duration of a single breathing cycle was 4.05 s, with 1.9 and 2.15 s taken up by inhalation and exhalation, respectively.

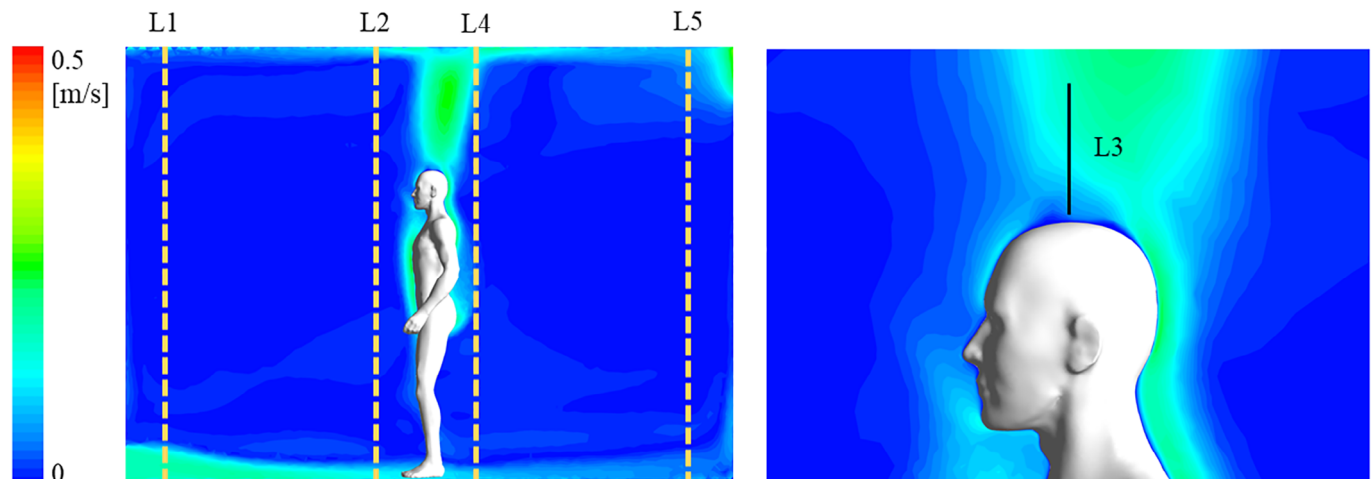


FIGURE 6. Scalar velocity field around the CSP and location of the sampled point

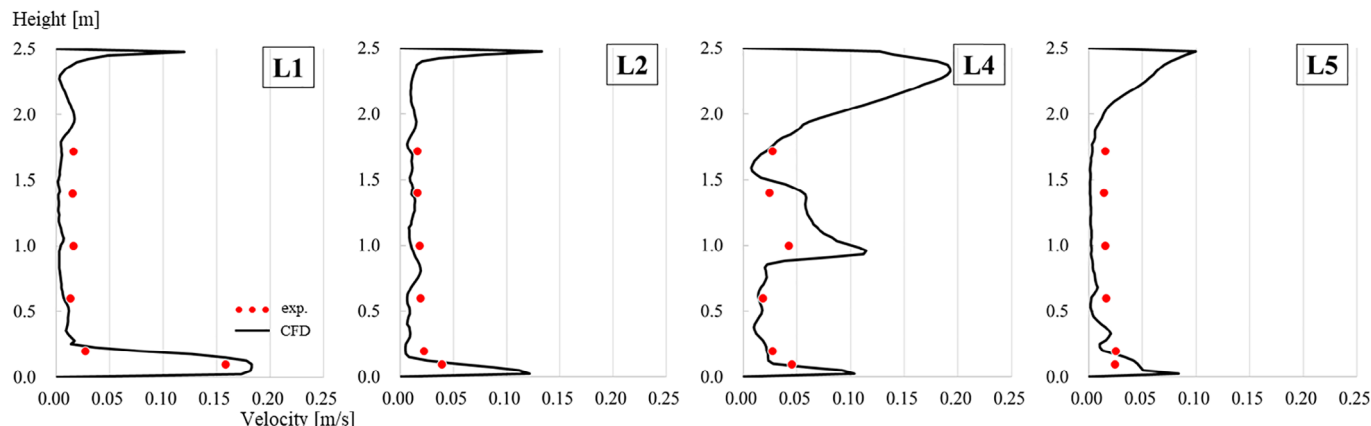


FIGURE 7. Experimental and CFD analysis-based velocity profiles for lines L1, L2, L4, and L5

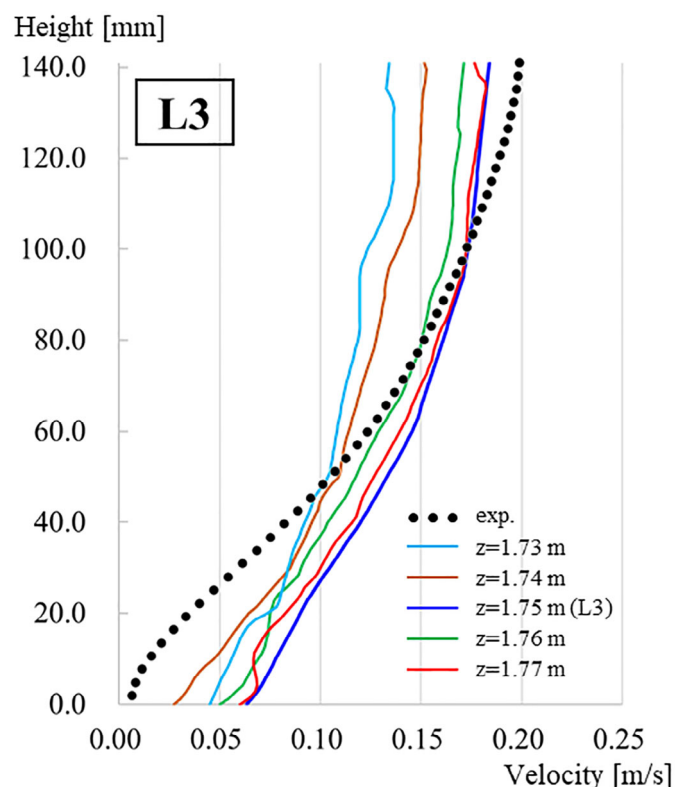


FIGURE 8. Experimental and CFD analysis-based velocity profiles for line L3

To incorporate the breathing function into the CSP based on an unsteady breathing cycle, nasal breathing was assumed in this study. The variation in the breathing flow rate was used as a boundary condition for the nostril surfaces of the CSP, and calculations for unsteady breathing were conducted using sufficiently small time-steps, to satisfy the Courant–Friedrichs–Lewy (CFL) condition. This study focused on the impact of unsteady breathing on (1) the airflow characteristics in the breathing zone and (2) development of human-generated thermal plumes. The flow field analysis results for the CSP proximity, with and without the reproduction of unsteady breathing, are summarized in Figure 10. When the CSP had no

breathing function incorporated, the airflow around the CSP owing to the complex human body geometry was only slightly non-uniform. When the CSP was in the maximal-inhalation mode (point (a) in Figure 9), high velocity was observed only in the vicinity of the CSP nostrils. Whereas no intense airflow was observed in the breathing zone when the CSP transitioned from inhalation to exhalation (point (b) in Figure 9), an exhalation jet was clearly formed at the maximal-exhalation point (point (c) in Figure 9), and gradually diffused over time. The exhalation jet affected the flow pattern in the region extending to approximately 0.25 m (along the horizontal axis) and 0.45 m (along the vertical axis) away from the CSP nostrils. These results revealed that the reproduction of unsteady breathing in the CSP analysis crucially affected the flow pattern in the breathing zone, and the CSP with unsteady breathing could be used for precise prediction of contaminant behavior in the breathing zone and for predicting the concentration levels of contaminant inhalation and respiratory exposure.

To investigate the impact of unsteady breathing on the development of human-generated thermal plumes, the velocity profiles for line L3 in Figure 6 during one breathing cycle were obtained and summarized in Figure 11. No significant differences between the velocity profiles during unsteady breathing were observed, indicating that the breathing jet did not strongly affect the global/local microclimate around the human body, except in the breathing zone.

This study assumed that a nasal breathing condition with a low breathing flow rate corresponds to a low metabolic rate during quiet standing as a general condition. Oronasal breathing, with higher breathing flow rates associated with heavy physical activity, may affect the flow characteristics around the human body; this will be addressed in future studies.

3.2 Human micromotion in the standing posture

Because two-thirds of the human body mass are concentrated in the two-thirds of the body height, the human body is inherently an unstable system.⁴² Micromotion owing to the posture control of the human body is always present, although it is age and health dependent.^{43–45} This study focused on the micromotion of the human body, and the impact on the microclimate around the human body was quantitatively analyzed.

In this study, an inverted pendulum model (IPM) was applied to the CSP, to investigate the impact of human micromotion on the microclimate around the human body.

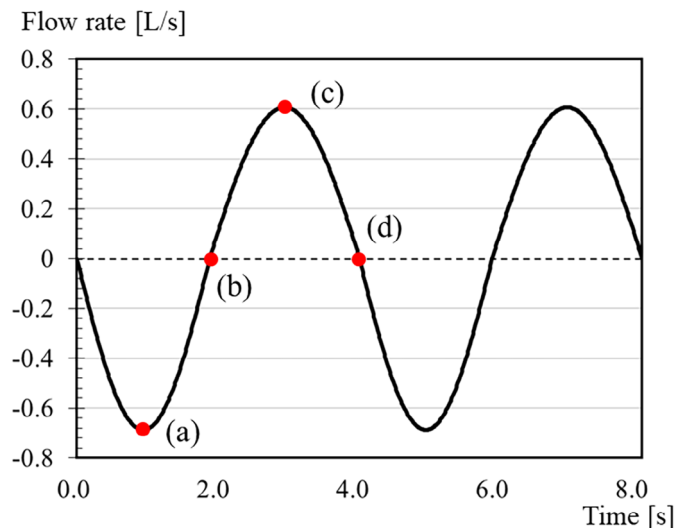


FIGURE 9. Variations in the breathing flow rate during unsteady breathing

Multisegment IPMs have been widely used for investigating the balance control of the human body. However, it was argued that a single-segment IPM, a simplified model that considers the pivot at the ankle only, also accurately predicts the sway motion of the human body.⁴⁶ In this study, a single-segment IPM was used for defining the sway angular velocity and sway frequency of the CSP during quiet standing. The single-segment IPM that was used in this study is schematically shown in Figure 12. Owing to the neuromuscular control for maintaining an upright posture, the human body sways in the anteroposterior (AP) and (b) mediolateral (ML) directions.

Many previous studies have investigated the nature of the human postural sway, using the measured center of pressure (COP) and center of mass (COM) of the human body.^{23,47–49} The relationship between COP, COM, COP minus COM, and the behavior of the postural sway of the human body has been studied.^{46,50,51} Based on this information, maximal angular velocity (ω_{max}) in the 3.0–5.0°/s range was assumed in this study, to investigate the effect of the general sway intensity (assuming young and healthy adults) on the human microclimate. As the fluctuation of COP, COM and COP minus COM in measured data corresponds to the postural sway frequency, we set 1.0 Hz for the AP direction and 0.5 Hz for the ML direction, based on the previously reported values.^{52–55} The angular velocity and sway frequency of the human body were simplified assuming a sine function, as shown in Figure 13A. As a result, the head displacements indicated in Figure 12 for

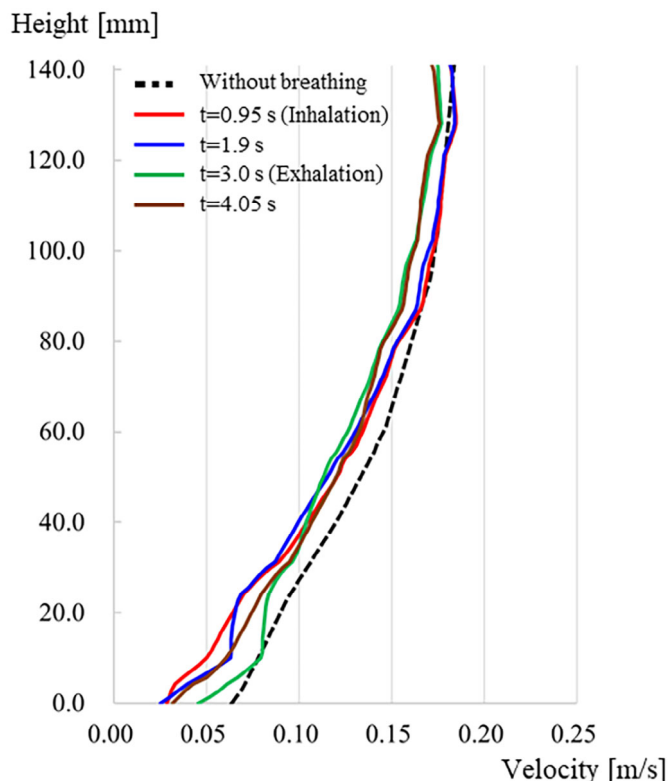


FIGURE 11. Velocity profiles for line L3, during unsteady breathing

$\omega_{max} = 3.0, 4.0,$ and 5.0 °/s were approximately 14.5, 19.3, and 24.1 mm, as summarized in Figure 13B; these values are typical for young and healthy adults.⁵⁶

A simple model room and the CSP shown in Figure 3 were used to investigate the reproducibility of the human micromotion effects in a human microclimate. Micromotion, as defined in Figure 13A, was applied to the CSP using a dynamic mesh in ANSYS Fluent 2021R2.⁵⁷ In this study, the convective heat transfer coefficient over the entire CSP surface was estimated for static and swaying conditions. The fixed surface temperature of the CSP was 33.55°C, with the environment temperature (inflow temperature) at 24.85°C. A uniform inflow from the anterior to posterior region was used (speed, 0.1 m/s), assuming a gentle airflow distribution in a general indoor environment.

As a numerical technique for reproducing the temporal dynamics of the human postural sway, a dynamic mesh with a smoothing method was applied to the analytical grids around the CSP, to respond to the angular translation of the CSP

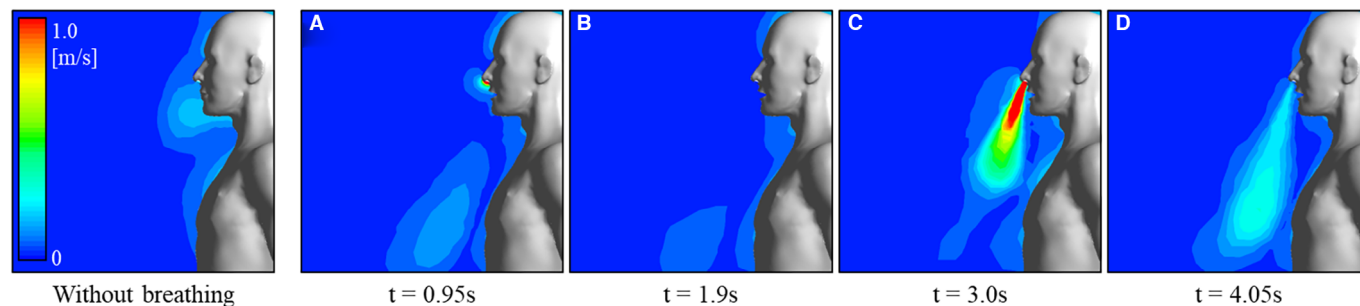


FIGURE 10. Scalar velocity distribution patterns in the breathing zone, during unsteady breathing

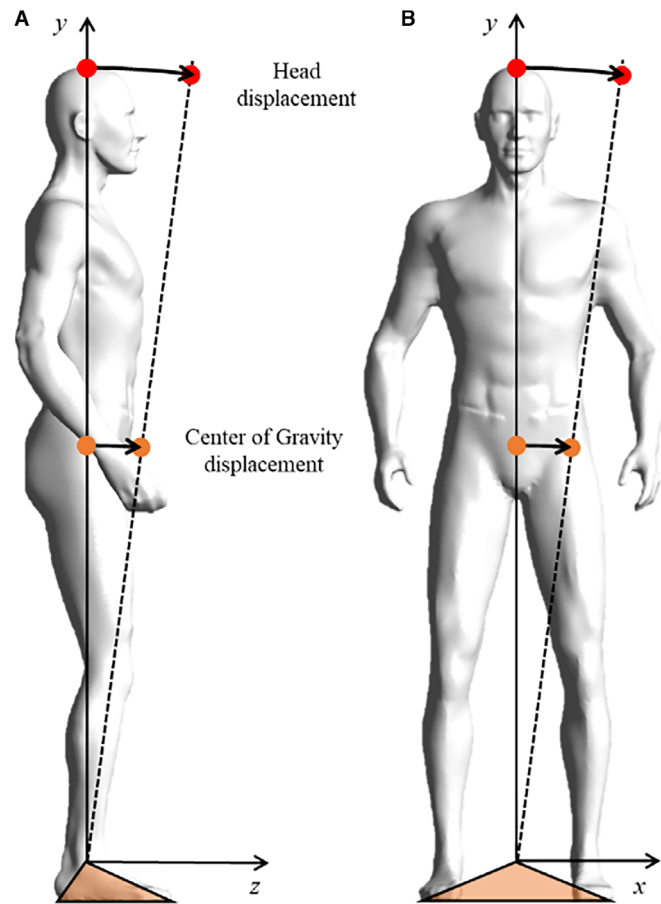


FIGURE 12. Schematic of the single-segment IPM and human postural sways in (A) the anterior–posterior (AP) and (B) medial-lateral (ML) directions

without remeshing. However, 10 layers of boundary meshes on the CSP were maintained, for analyzing the numerical error owing to the boundary mesh variations. The SIMPLE algorithm was used for the pressure–velocity coupling. The SST $k-\omega$ model was used for turbulence calculations, and a second-order upwind scheme was used for the convection term. To ensure the stability and convergence of calculations, the time-step was set to a sufficiently small value of 0.005 s.

Figure 14 shows some representative results of the analysis of the scalar velocity distribution around the CSP, with and without the postural sway, for $\omega_{max} = 4.0$ °/s and $t = 90.0$ s. The global flow field in the indoor space and the thermal plume around the CSP are not critically affected by the human micromotion. In contrast, a discrepancy between the velocity distributions near the CSP surface is clearly observed, for both the AP and ML directions. However, Figure 14 shows a snapshot at $t = 90.0$ s, and does not inform about the steady-state distribution.

To quantitatively investigate the impact of micromotion on the CSP, the time-averaged convective heat transfer coefficient on the CSP surface was calculated using parametric analyses, for various values of the maximal angular velocity ($\omega_{max} = 3.0, 4.0,$ and 5.0), and the results are summarized in Figure 15. With postural sway, the convective heat transfer coefficient on the CSP surface increased by 0.09, 0.27, and 1.7% for $\omega_{max} = 3.0, 4.0,$ and 5.0 °/s, respectively. Although higher convective heat transfer coefficients were observed for higher maximal angular velocities, these results imply that the impact of micromotion on the convective heat and mass transfer of

the CSP is negligible. Young and healthy adults were assumed in this parametric analysis that sought to determine the impact of the maximal angular velocity, with more intense postural sway corresponding to less stable quiet standing. Thus, elderly people or humans with balance disorders may stronger affect both human microclimate and convective heat/mass transfer of the human body.

4. Validation and Verification of the Respiratory Tract Model

By performing contaminant transfer analysis for indoor spaces and the respiratory tract, specific health risks owing to the inhalation of contaminants can be estimated. This study used a numerical respiratory tract model that was originally developed in our previous studies; using the model, we sought to validate the flow/contaminant transfer analysis in the human respiratory tract model.^{58,59} In this study, the grid independence of the respiratory tract model was carefully checked, and the analysis results for the airflow and deposition of particles obtained using the optimal grid design were validated against available experimental data.

4.1 Outline of the respiratory tract model

A computational human respiratory tract model was originally developed in our previous studies based on computed tomography (CT) data obtained from a non-smoking and healthy Asian male. As shown in Figure 16A, the detailed geometries, from

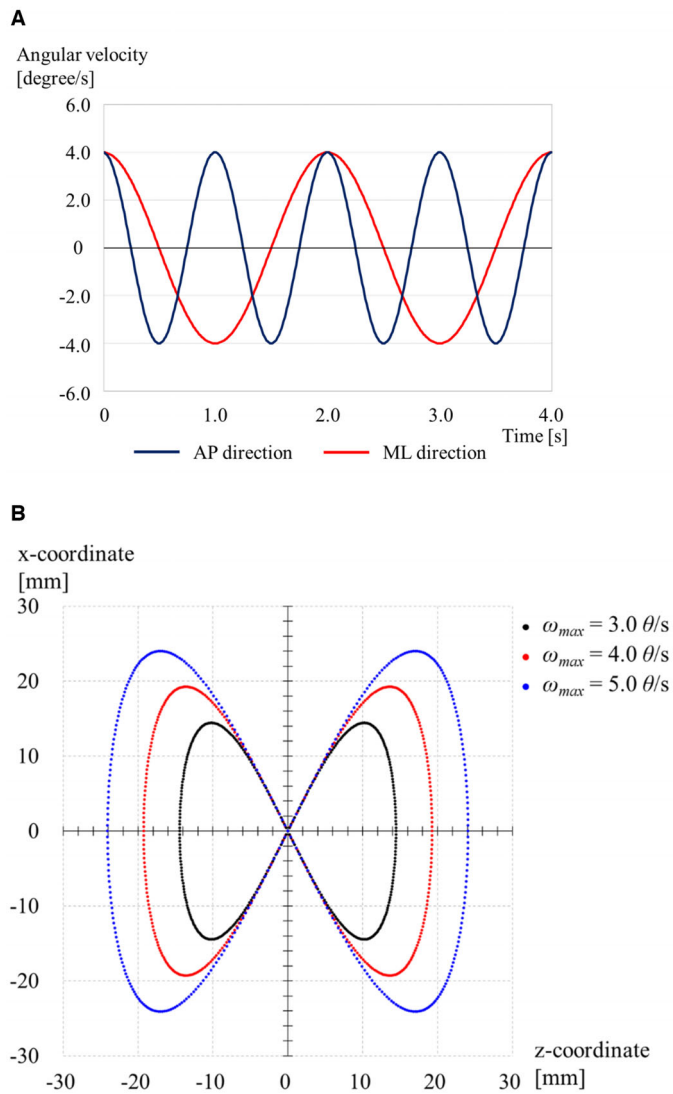


FIGURE 13. (A) Angular velocity of the CSP in the AP and ML directions, vs. time, for $\omega_{max} = 4.0 \text{ }^\circ/s$ and (B) head displacement at each time step ($\Delta t = 0.005 \text{ s}$), for three different maximal angular velocities

the nasal/oral cavity to the fourth bifurcation of the bronchial tubes, were extracted. The height and volume of the respiratory tract model were approximately 34.8 cm and 173 cm³, respectively. Figure 16B shows the representative grid design

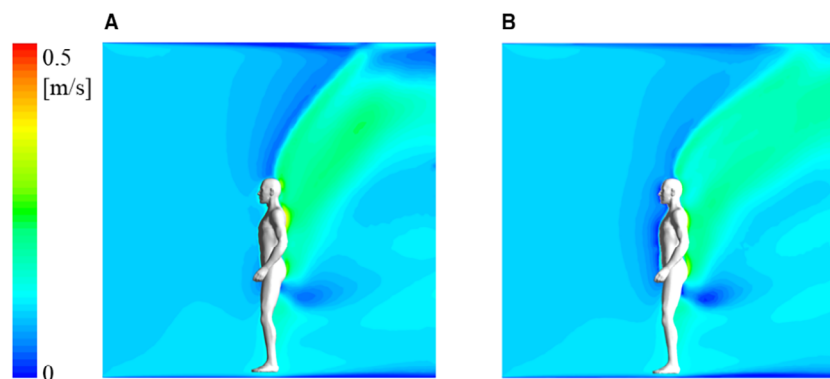


FIGURE 14. Scalar velocity distributions near the CSP (A) with and (B) without postural sway, for $\omega_{max} = 4.0^\circ/s$ and $t = 90.0 \text{ s}$

Convective heat transfer coefficient [W/m²K]

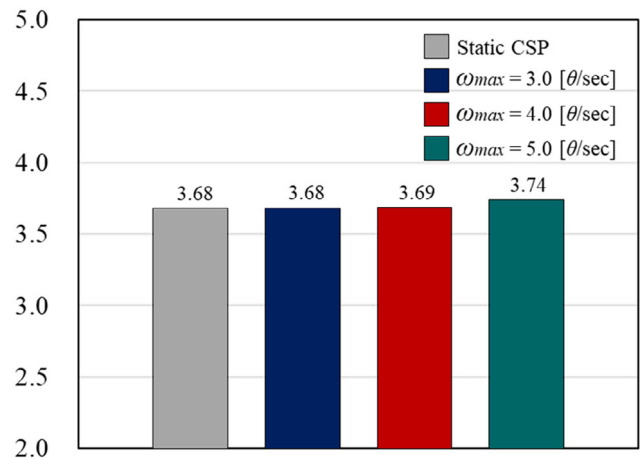


FIGURE 15. Time-averaged convective heat transfer coefficient on the CSP surface, for $\omega_{max} = 3.0, 4.0,$ and $5.0^\circ/s$

of the numerical respiratory tract model (7.5 million tetrahedral cells).

4.2 Grid independence test on the respiratory tract model

To check the grid independence of the numerical respiratory tract model based on the flow field analysis, this study focused on the flow pattern in the trachea region, which exhibits a well-developed flow compared with other regions. The scalar velocity profiles in the A-A' section in Figure 16A were obtained from the flow field analysis using four different grid designs: 1.0 million, 4.6 million, 7.5 million, and 10.6 million tetrahedral cells. For the flow field analysis, the inhalation air-flow rate was 7.5 L/min, and the second-order upwind scheme for the convection term and the SIMPLE algorithm were used. Figure 17 summarizes the mean scalar velocity profile for the A-A' section, calculated using the four different grid designs. Considering the peak velocity and overall distribution of the velocity in this section, the grid design with 7.5 million tetrahedral cells was found to be the optimal one; consequently, this grid design was used for benchmarking.

4.3 Validation of the flow field analysis in the respiratory tract model

To examine the prediction accuracy and reproducibility of the flow pattern in the respiratory tract, a three-dimensional replica

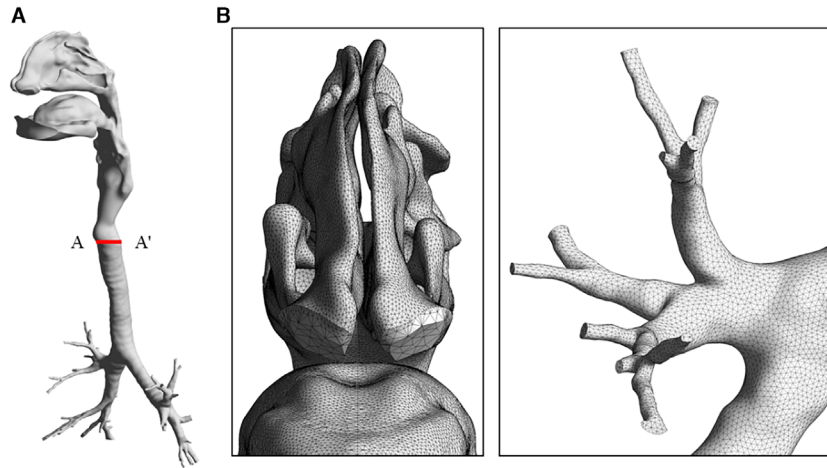


FIGURE 16. Outline of the geometrical data and the representative grid design of the respiratory tract model

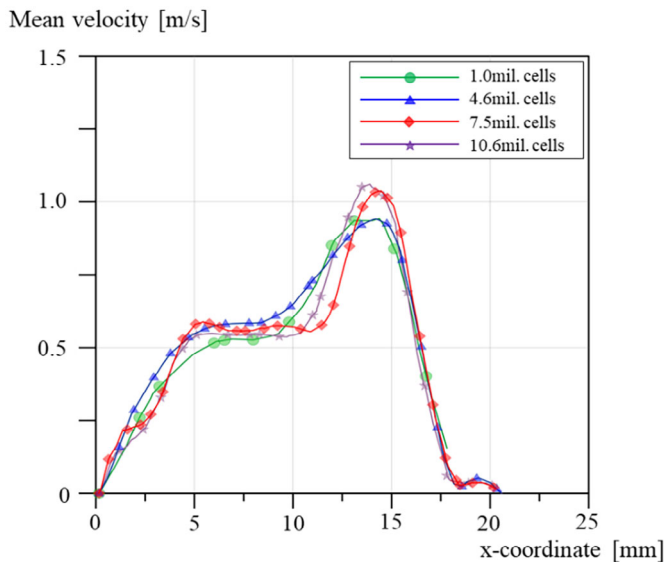


FIGURE 17. Scalar velocity profile, for the A-A' section

model was designed, based on the geometrical data of the respiratory tract model, and detailed information on the velocity distribution in the respiratory tract was obtained from PIV data. Figure 18 shows the experimental setup for PIV measurements. The flow pattern in the trachea region was measured assuming the Reynolds number of approximately 500, which corresponds to the breathing airflow rate of 7.5 L/min.

It is essential to clarify the impact of a specific turbulence model on the prediction accuracy of the flow distribution, considering the turbulent flow caused by the complex geometrical structure of the respiratory tract. For CFD simulations of the respiratory tract, two turbulence models were used: (1) a low-Reynolds-number $k-\epsilon$ model and (2) an SST $k-\omega$ model.^{31,60,61} A grid design of 7.5 million cells was used, and the cells nearest to the surface were assumed to be in a viscous sublayer, by arranging sufficiently small cells near the surface. As a result, the dimensionless distance to the surface (y^+) was below 1.0 over the entire surface in the respiratory tract model.

The normalized velocity profiles for section B-B' obtained by numerical analysis and from experimental data are summarized in Figure 19. Good consistency was confirmed between

the results of the PIV experiment and CFD analysis performed using the methodology in this study; the calculation results using the SST $k-\omega$ model better agreed with the experimental results.

4.4 Validation of the particle deposition analysis in the respiratory tract model

The main objective of the respiratory tract's microclimate analysis was to quantitatively and qualitatively predict indoor health risks through a respiratory exposure assessment. To use the numerical respiratory tract model for assessing health risks, it is important to confirm the prediction accuracy of the inhalation risk assessment of indoor contaminants. In this work, we simulated particulate contaminant inhalation using the respiratory tract model, and compared the results with previously reported in vivo measurements.

Discrete-phase particle transport analysis was conducted using the Euler-Lagrange method, assuming the inhalation of spherical particles. Flow field analysis of the respiratory tract was conducted based on the methodology established in this study, and overall 10 000 particles were injected through the CSP nostrils. The particles' density was $\rho_p = 1000 \text{ [kg/m}^3\text{]}$, in accordance with the definition of the particles' aerodynamic diameter. The escape and trap boundary conditions for treating the particles were applied to the inlet/outlet and wall surfaces in the respiratory tract model, respectively. The total deposition fraction (η) in the respiratory tract was calculated using Equation (6), with C_{WD} indicating the total number of particles deposited on the entire surface of the respiratory tract, and C_{in} denoting the total number of inhaled particles.

$$\eta = \frac{C_{WD}}{C_{in}} \times 100\%. \tag{6}$$

The inertial parameter (IP) was used to discuss the deposition of micron-sized particles in the respiratory tract.⁶² IP is defined by Equation (7), considering the particles' aerodynamic diameter (d_a) and inhalation airflow rate (Q_{in}).

$$IP = d_a^2 \cdot Q_{in}. \tag{7}$$

The value of d_a was varied in the 1–10 μm range, while the value of Q_{in} was varied in the 7.5–60 L/min range, to study

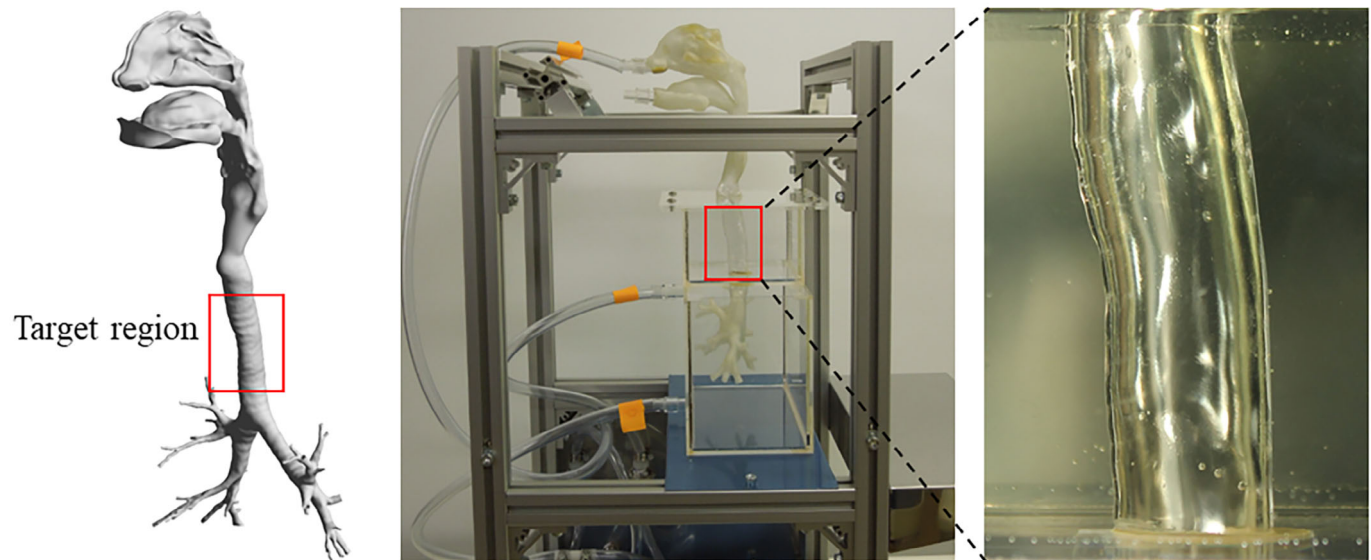


FIGURE 18. Experimental setup for PIV measurements using a replica model

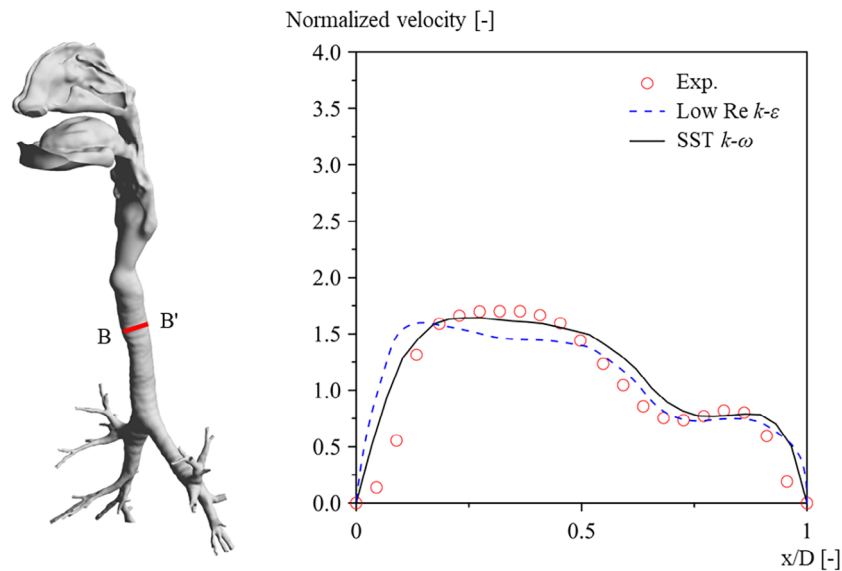


FIGURE 19. Normalized velocity profiles for section B-B', obtained from PIV experiments and CFD analyses

the dependence of the deposition behavior on the particles' diameter and flow characteristics. The analysis results were compared with the previously published results of in vivo measurements.^{63,64}

Figure 20 compares the deposition fraction obtained in the present study with previously reported values. Both the previously reported and the currently estimated data exhibit sigmoidal-like trends. The numerical analysis results obtained using the methods in the present study were largely concordant with previously published experimental data, with a small discrepancy owing to anatomical differences between the respiratory tracts used in the different studies, which is not accounted for by the IP.

5. Limitations of this Study

Modeling the morphology of the human body and the physiological/psychological mechanisms associated with heating,

ventilation, and air conditioning changes has been an important research topic. Over the past few decades, CSPs have been introduced into the CFD analysis of indoor airflows. An important objective of a CSP in a CFD framework is to enable the analysis of the skin surface temperature distribution by analyzing the local convective and radiative heat flux on the skin surface in the context of a specific indoor environment. Therefore, it is important to model clothing in terms of heat and mass transfer resistance, for accurate estimations of the skin surface temperature distribution. The ventilation in the air layer formed between the human body and clothing and the heat and mass transfer therein have complex geometries. To address this issue, an idealistic modeling approach that concentrates the resistance on the surface layer, or a realistic modeling approach that creates an exhaustive clothing model that directly reproduces the airflow, heat, and mass transfer in the clothing air layer, have been proposed. We note that clothing

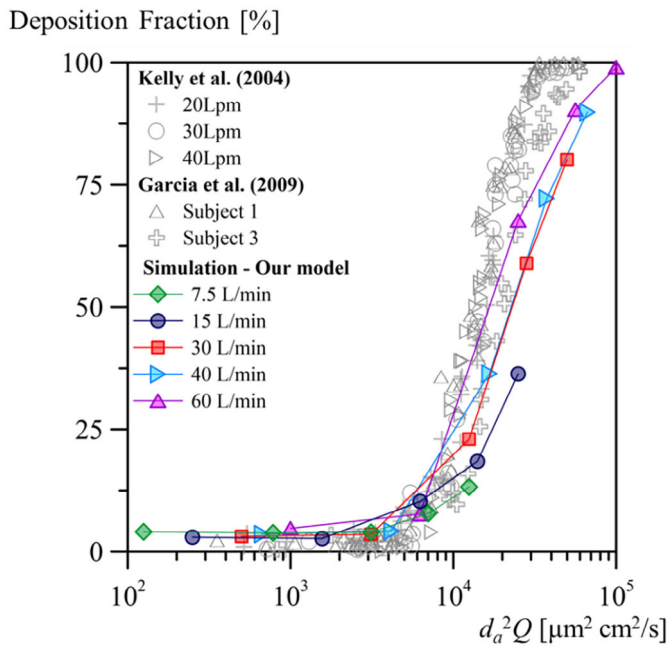


FIGURE 20. Comparison of the numerically estimated particle deposition fraction (using the numerical respiratory tract model in the present study) and previously reported in vivo measurement results

modeling is beyond the scope of the present report, but should be addressed in future studies.

In terms of the skin surface temperature control, the development of a thermoregulation model for the human body is also an important issue. Various types of thermoregulation models, such as the Fiala, Stolwijk, JOS, and Smith models, have been proposed for integration with CFD analysis. The choice of the thermo-regulation model is expected to significantly affect the results of the analysis of the metabolic heat generation by the human body and the air temperature distribution around the human body.

For successful predictions of airborne transmission in indoor environments, the transport of droplets and droplet nuclei (generated by infected individuals) to the breathing zone of susceptible indoor residents must be precisely analyzed. The flow field around the breathing zone may be significantly influenced by transient breathing cycles, coughing, and sneezing. These can be categorized as unsteady jets generated by the nostrils or mouth, and require accurate modeling in terms of predicting the flow field around the human body. This study discussed the impact of transient breathing on the flow patterns in the breathing zone.

Although we omitted the discussion of thermo-regulation modeling and cough and sneezing modeling in this study, it will be a very important issue in terms of the CFD analysis of indoor environments using CSPs.

6. Conclusion

This study introduced a CSP with a numerical respiratory tract model established for a detailed IEQ assessment based on the CFD analysis. To provide useful information for the quality control of the IEQ assessment using the CSP, this study validated the prediction accuracy of indoor global/local climate analysis using the CSP, by performing sophisticated

grid independence and benchmarking tests. As a result, satisfactory concordance was confirmed between the results of the indoor flow field analysis using a CSP with a grid design of $R^* = 12$ and the SST $k-\omega$ turbulence model. Based on the methodology of the CSP analysis established in this study, the impact of unsteady breathing and human micromotion during quiet standing on the microclimate around the human body was also investigated, and the negligible impact of breathing and postural sway on the human thermal plume was confirmed.

In addition, verification and validation of the flow and contaminant transfer analysis in the respiratory tract were conducted. As a result, the flow field analysis using the grid with 7.5 million tetrahedral cells and the SST $k-\omega$ turbulence model exhibited good reproducibility of the experimental results. This study also examined the prediction accuracy of particle transport and deposition analysis in the respiratory tract, for applying the respiratory tract model to the inhalation risk analysis with IAQ problems, and good concordance between the numerical analysis results and in vivo experimental data was observed. Although there is potential for improving the benchmarking test results of the CSP, this study confirmed sufficient reproducibility. The CSP analysis methods discussed in this study are likely to be useful for advanced IEQ assessments and sophisticated indoor environmental designs.

Acknowledgements

This research was partially funded by the Japan Science and Technology (JST), CREST Japan (grant number JP 20356547), and the Japan Society for the Promotion of Science (JSPS) Grants-in-Aid for Scientific Research (KAKENHI) (grant numbers JP20KK0099, JP21K14306, JP22H00237), Health Labour Sciences Research Grant (JP 21KD2002), MEXT as “Program for Promoting Researches on the Supercomputer Fugaku” (grant number JPMXP1020210316), and The Taisei Foundation Research Grant (grant number 20015). The authors would like to express special thanks to the benefactors.

Disclosure

The authors declare that they have no competing financial interests or personal relationships that could have influenced the work reported in this paper.

DATA AVAILABILITY STATEMENT

The data that support the findings of this study are available from the corresponding author upon reasonable request.

References

- Xing H, Hatton A, Awbi HB. A study of the air quality in the breathing zone in a room with displacement ventilation. *Build Environ.* 2001;**36**(7):809-820.
- Brohus H. *Personal Exposure to Contaminant Sources in Ventilated Rooms*, Ph.D. Thesis. Aalborg University; 1997.
- Brohus H, Balling KD, Jeppesen D. Influence of movements on contaminant transport in an operating room. *Indoor Air.* 2006;**16**:356-372. doi:10.1111/j.1600-0668.2006.00454.x
- Murakami S, Zeng J. Flow and temperature fields around human body with various room air distributions, part 1 -CFD study on computational thermal manikin. *AHSRAE Trans.* 1997;**103**:3-15.
- Murakami S, Kato S, Zeng J. Combined simulation of airflow, radiation and moisture transport for heat release from human body. *Build Environ.* 2000;**35**:489-500.
- Edge BA, Paterson EG, Settles GS. Computational study of the wake and contaminant transport of a walking human. *ASME. J. Fluids Eng.* 2005;**127**(5):967-977. doi:10.1115/1.2013291

- 7 Topp C, Nielsen PV, Sørensen DN. Application of computer-simulated persons in indoor environmental modeling. *ASHRAE Trans.* 2002;**108**(Pt. 2):2002.
- 8 Sorensen DN, Voigt LK. Modeling flow and heat transfer around a seated human body by computational fluid dynamics. *Build Environ.* 2003;**38**(6):753-762.
- 9 Choi J-I, Edwards JR. Large eddy simulation and zonal modeling of human-induced contaminant transport. *Indoor Air.* 2008;**18**:233-249. doi:10.1111/j.1600-0668.2008.00527.x
- 10 Gao NP, Zhang H, Niu JL. Investigating indoor air quality and thermal comfort using a numerical thermal manikin. *Indoor Built Environ.* 2007;**16**(1):7-17.
- 11 Nielsen PV, Murakami S, Kato S, Topp C, Yang J-H. *Benchmark Tests for a Computer Simulated Person.* Aalborg University, Indoor Environmental Engineering; 2003.
- 12 Tao Y, Yang W, Inthavong K, Jiyuan T. Indoor particle inhalability of a stationary and moving manikin. *Build Environ.* 2020;**169**:106545. doi:10.1016/j.buildenv.2019.106545
- 13 Kuga K, Wargocki P, Ito K. Breathing zone and exhaled air re-inhalation rate under transient conditions assessed with a computer-simulated person. *Indoor Air.* 2022;**32**:e13003. doi:10.1111/ina.13003
- 14 Dang Khoa N, Phuonng NL, Takahashi K, Ito K. Transport and deposition of inhaled man-made vitreous and asbestos fibers in realistic human respiratory tract models: an in silico study. *Jpn Archit Rev.* 2022. doi:10.1002/2475-8876.12277
- 15 Inthavong K, Shang Y, Del Gaudio JM, et al. Inhalation and deposition of spherical and pollen particles after middle turbinate resection in a human nasal cavity. *Respir Physiol Neurobiol.* 2021;**294**:103769. doi:10.1016/j.resp.2021.103769
- 16 Salati H, Khamooshi M, Vahaji S, Christo FC, Fletcher DF, Inthavong K. N95 respirator mask breathing leads to excessive carbon dioxide inhalation and reduced heat transfer in a human nasal cavity. *Phys Fluids.* 2021;**33**:081913. doi:10.1063/5.0061574
- 17 Dong J, Shang Y, Tian L, Inthavong K, Qiu D, Tu J. Ultrafine particle deposition in a realistic human airway at multiple inhalation scenarios. *Int J Numer Meth Biomed Eng.* 2019;**35**:e3215. doi:10.1002/cnm.3215
- 18 Tian L, Shang Y, Chen R, et al. A combined experimental and numerical study on upper airway dosimetry of inhaled nanoparticles from an electrical discharge machine shop. *Part Fibre Toxicol.* 2017;**14**:24. doi:10.1186/s12989-017-0203-7
- 19 Tu J, Inthavong K, Ahmadi G. *Computational Fluid and Particle Dynamics in the Human Respiratory System.* Springer; 2012.
- 20 Tian L, Shang Y, Dong J, Inthavong K, Jiyuan T. Human nasal olfactory deposition of inhaled nanoparticles at low to moderate breathing rate. *J Aerosol Sci.* 2017;**113**:189-200. doi:10.1016/j.jaerosci.2017.08.006
- 21 Li X, Inthavong K, Tu J. Particle inhalation and deposition in a human nasal cavity from the external surrounding environment. *Build Environ.* 2016;**47**(1):32-39.
- 22 Inthavong K, Ge Q, Li X, Tu J. Detailed predictions of particle aspiration affected by respiratory inhalation and airflow. *Atmos Environ.* 2012;**62**:107-117.
- 23 Panzer VP, Bandinelli S, Hallett M. Biomechanical assessment of quiet standing and changes associated with aging. *Arch Phys Med Rehabil.* 1995;**76**(2):151-157. doi:10.1016/s0003-9993(95)80024-7
- 24 Luo N, Weng W, Xu X, Fu M. Human-walking-induced wake flow – PIV experiments and CFD simulations. *Indoor Built Environ.* 2018;**8**:1069-1084. doi:10.1177/1420326X17701279
- 25 Tao Y, Inthavong K, Tu J. Computational fluid dynamics study of human-induced wake and particle dispersion in indoor environment. *Indoor Built Environ.* 2017;**26**(2):185-198. doi:10.1177/1420326X16661025
- 26 Hang J, Li Y, Jin R. The influence of human walking on the flow and airborne transmission in a six-bed isolation room: tracer gas simulation. *Build Environ.* 2014;**77**:119-134. doi:10.1016/j.buildenv.2014.03.029
- 27 Luo N, Weng WG, Fu M, Yang J, Han ZY. Experimental study of the effects of human movement on the convective heat transfer coefficient. *Exp Therm Fluid Sci.* 2014;**57**:40-56. doi:10.1016/j.exthermfluidsci.2014.04.001
- 28 Ito K. Toward the development of an in silico human model for indoor environmental design. *Proc Jpn Acad Ser B.* 2016;**92**(7):185-203.
- 29 Yoo SJ, Ito K. Numerical prediction of tissue dosimetry in respiratory tract using computer simulated person integrated with physiologically based pharmacokinetic-computational fluid dynamics hybrid analysis. *Indoor Built Environ.* 2018;**27**(7):877-889.
- 30 Lee M, Park G, Park C, Kim C. Improvement of grid Independence test for computational fluid dynamics model of building based on grid resolution. *Adv Civ Eng.* 2020;**2020**:8827936. doi:10.1155/2020/8827936
- 31 Menter FR, Kuntz M, Langtry R. Ten years of industrial experience with the SST turbulence model. In: Hanjalic K, Nagano Y, Tummers M, eds. *Turbulence, Heat and Mass Transfer.* Vol 4. Begell House Inc; 2003:625e632.
- 32 Sorensen DN, Nielsen PV. Quality control of computational fluid dynamics in indoor environments. *Indoor Air.* 2003;**13**:2-17.
- 33 Foat TG, Parker ST, Castro IP, Xie Z-T. Numerical investigation into the structure of scalar plumes in a simple room. *J Wind Eng Ind Aerodyn.* 2018;**175**:252-263.
- 34 Nielsen PV. *Specification of a Two-dimensional Test Case: (IEA), Vol. 1 (No. 8).* Institut for Bygningsteknik, Aalborg UniversitetR9040 [Gul serie]; 1990.
- 35 Nielsen PV. Fifty years of CFD for room air distribution. *Build Environ.* 2015;**91**:78-90.
- 36 Ito K, Inthavong K, Kurabuchi T, et al. CFD benchmark tests for indoor environmental problems: part 1 isothermal/non-isothermal flow in 2D and 3D room model. *J Archit Eng Technol.* 2015;**2**(1):1-22.
- 37 Ito K, Inthavong K, Kurabuchi T, et al. CFD benchmark tests for indoor environmental problems: part 4 air-conditioning airflows, residential kitchen airflows and fire-induced flow. *J Archit Eng Technol.* 2015;**2**(1):76-102.
- 38 Ito K, Inthavong K, Kurabuchi T, et al. CFD benchmark tests for indoor environmental problems: part 3 numerical thermal manikins. *J Archit Eng Technol.* 2015;**2**(1):50-75.
- 39 Ito K, Inthavong K, Kurabuchi T, et al. CFD benchmark tests for indoor environmental problems: part 2 cross-ventilation airflows and floor heating systems. *J Archit Eng Technol.* 2015;**2**(1):23-49.
- 40 ASHRAE. *ASHRAE Guideline 14: Measurement of Energy and Demand Savings.* American Society of Heating, Refrigerating and Air-Conditioning Engineers Inc; 2002.
- 41 Gupta JK, Lin CH, Chen Q. Characterizing exhaled airflow from breathing and talking. *Indoor Air.* 2009;**20**:31-39.
- 42 Winter DA. Human balance and posture control during standing and walking. *Gait Posture.* 1995;**3**(4):193-214. doi:10.1016/0966-6362(96)82849-9
- 43 Davidson BS, Madigan ML, Southward SC, Nussbaum MA. Neural control of posture during small magnitude perturbations: effects of aging and localized muscle fatigue. *IEEE Trans Biomed Eng.* 2011;**58**(6):1546-1554. doi:10.1109/TBME.2010.2095500
- 44 Doheny EP, McGrath D, Greene BR, et al. Displacement of Centre of mass during quiet standing assessed using accelerometry in older fallers and non-fallers. *Proceedings of the Annual International Conference of the IEEE Engineering in Medicine and Biology Society.* EMBS; 2012:3300-3303. doi:10.1109/EMBC.2012.6346670
- 45 Collins JJ, de Luca CJ. Open-loop and closed-loop control of posture: a random-walk analysis of center-of-pressure trajectories. *Exp Brain Res.* 1993;**95**(2):308-318. doi:10.1007/BF00229788
- 46 Morasso P, Cherif A, Zenzeri J. Quiet standing: the single inverted pendulum model is not so bad after all. *PLoS ONE.* 2019;**14**(3):e0213870. doi:10.1371/journal.pone.0213870
- 47 do Carmo AA, Kleiner AFR, Barros RML. Alteration in the center of mass trajectory of patients after stroke. *Top Stroke Rehabil.* 2015;**22**(5):349-356. doi:10.1179/1074935714Z.0000000037
- 48 Fujio K, Takeuchi Y. Discrimination of standing postures between young and elderly people based on center of pressure. *Sci Rep.* 2021;**11**(1):195. doi:10.1038/s41598-020-80717-z
- 49 Kingma I, Toussaint HM, Commissaris DACM, Hoozemans MJM, Ober MJ. Optimizing the determination of the body center of mass. *In J Biomechanics.* 1995;**28**(9):1137-1142.
- 50 Masani K, Vette AH, Abe MO, Nakazawa K. Center of pressure velocity reflects body acceleration rather than body velocity during quiet standing. *Gait Posture.* 2014;**39**(3):946-952. doi:10.1016/j.gaitpost.2013.12.008
- 51 Masani K, Vette AH, Kouzaki M, Kanehisa H, Fukunaga T, Popovic MR. Larger center of pressure minus center of gravity in the elderly induces larger body acceleration during quiet standing. *Neurosci Lett.* 2007;**422**(3):202-206. doi:10.1016/j.neulet.2007.06.019 Epub 2007 Jun 17. PMID: 17611029.
- 52 Hasan SS, Robin DW, Szurkus DC, Ashmead DH, Peterson SW, Shiavi RG. Simultaneous measurement of body center of pressure and center of gravity during upright stance. Part II: amplitude and frequency data. *Gait Posture.* 1996;**4**(1):11-20. doi:10.1016/0966-6362(95)01031-9
- 53 Sakanaka TE, Lakie M, Reynolds RF. Idiosyncratic characteristics of postural sway in Normal and perturbed standing. *Front Hum Neurosci.* 2021;**15**:660470. doi:10.3389/fnhum.2021.660470
- 54 Latash ML, Ferreira SS, Wiecek SA, Duarte M. Movement sway: changes in postural sway during voluntary shifts of the center of pressure. *Exp Brain Res.* 2003;**150**(3):314-324. doi:10.1007/s00221-003-1419-3
- 55 Winter DA, Patla AE, Prince F, Ishaq M, Giello-Periczak K. Stiffness control of balance in quiet standing. *J Neurophysiol.* 1998;**80**(3):1211-1221.
- 56 Ciria LF, Muñoz MA, Gea J, et al. Head movement measurement: an alternative method for posturography studies. *Gait and Posture.* Vol 52. Elsevier B.V; 2017:100-106. doi:10.1016/j.gaitpost.2016.11.020
- 57 ANSYS/Fluent. *2021R1 User's Guide.* ANSYS Inc; 2021.
- 58 Phuong NL, Ito K. Investigation of flow pattern in a realistic replica model of human respiratory tract using PIV. *Build Environ.* 2015;**94**:504-515.

- 59 Phuong NL, Yamashita M, Yoo SJ, Ito K. Prediction of convective heat transfer coefficient of human upper and lower airway surfaces in steady and unsteady breathing conditions. *Build Environ*. 2016;**100**:172-185.
- 60 Abe K, Kondo T, Nagano Y. A new turbulent model for predicting fluid flow and heat transfer in separating and reattaching flows-1. Flow fields calculations. *Intl J Heat Mass Transfer*. 1994;**37**:139-151.
- 61 Abe K, Kondo T, Nagano Y. A new turbulent model for predicting fluid flow and heat transfer in separating and reattaching flows-2. Thermal fields calculations. *Intl J Heat and Mass Transfer*. 1995;**38**:1467-1481.
- 62 Hsu DJ, Chuang MH. In-vivo measurements of micrometer-sized particle deposition in the nasal cavities of Taiwanese adults. *Aerosol Sci Tech*. 2012;**46**(6):631-638. doi:[10.1080/02786826.2011.652749](https://doi.org/10.1080/02786826.2011.652749)
- 63 Kelly JT, Asgharian B, Kimbell JS, Wong BA. Particle deposition in human nasal airway replicas manufactured by different methods. Part I: inertial regime particles. *Aerosol Sci Tech*. 2004;**38**:1063-1071.
- 64 Garcia GJM, Tewksbury EW, Wong BA, Kimbell JS. Interindividual variability in nasal filtration as a function of nasal cavity geometry. *J Aerosol Med Pulm Drug Deliv*. 2009;**22**:139-155.

How to cite this article: Yoo S, Ito K. Validation, verification, and quality control of computational fluid dynamics analysis for indoor environments using a computer-simulated person with respiratory tract. *Jpn Archit Rev*. 0000;00:1–14. <https://doi.org/10.1002/2475-8876.12301>